Discontinuous Galerkin Method Applied To Critical Phenomena In Gravitational Collapse

Sean Johnson[a], Sylvia Mesicek[a], John Belz[a]

[a]*Department of Physics and Astronomy, University of Utah, 270 S 1400 E #E2108, Salt Lake City, 84112, UT, USA*

Abstract

A comparison between Discontinuous Galerkin and Finite Difference methods for solving critical phenomena in gravitational collapse of spherically symmetric massless scalar fields is performed. This is the first direct comparison between the two methods for critical phenomena in gravitational collapse. Through the use of the deal.II library, Discontinuous Galerkin methods are shown to require less degrees of freedom on average and require approximately half as many computational steps when compared to Finite Difference methods near criticality. These benefits address issues of run time and resolution found in Finite Difference simulations of higher dimension and more complicated fields. Application of the Discontinuous Galerkin method to gravitational collapse of nonlinear axisymmetric gravitational waves will be described in a future paper.

Keywords: Discontinuous Galerkin, Numerical Relativity, Critical Phenomena, Finite Difference, Adaptive Mesh, General Relativity

1. Introduction

General Relativity (GR) has been remarkably successful in precisely describing gravitational effects on all observed scales. These include phenomena within the solar system [1], binary pulsar timing [2, 3], gravitational wave observations [4] and large-scale cosmological structure [5].

Nevertheless, some predictions associated with the extreme spacetimes resulting in the formation of black holes call into question the viability of GR as a final theory. For example, the inevitability of singularities [6, 7] indicates a breakdown of classical spacetime and suggests the need for a quantum theory of gravity [8, 9]. Penrose [10] proposed the cosmic censorship conjecture,

according to which these singularities are always contained within a black hole's event horizon and thus can have no observable consequences. While this conjecture appears to be at least *nearly* true, evidence from theoretical and numerical studies [8, 11, 12, 13, 14, 15] point to the possibility of naked singularity formation under specific non-generic initial conditions.

Indeed, given the infeasibility of laboratory-based experimentation on black holes, numerical "thought experiments" currently provide the best testing ground for the most extreme predictions of General Relativity.

In 1993, Choptuik's seminal paper on critical phenomena in gravitational collapse of a massless scalar field in spherical symmetry [12] identified an infinitesimal point in phase-space in which this simple system could yield a naked singularity. Near this point, black holes can be created with a mass that scales as

$$M_{BH} \backsimeq c_f |p - p^*|^\gamma \tag{1}$$

where p is a parameter of the initial data that defines the phase space and p^* is the infinitesimal point that separates black hole formation and dispersion. The critical exponent, γ, is universal and was originally measured to be $\gamma \approx 0.37$.

In the region of strong field interaction, the solution also begins to exhibit discrete self similarity which is again universal. Choptuik originally referred to this phenomena as echoing. To match the exponential scale of self similarity, Choptuik used logarithmic variables

$$\rho = ln(r) \tag{2}$$

$$\tau = ln(T^* - t) \tag{3}$$

where T^* is the collapse time of the field parameterized by p^* as experienced by a central observer. The discrete spacing, Δ, between successive self similar moments, or echoes, was measured to be $\Delta \approx 3.44$.

The interplay of mass scaling and discrete self similarity led both Hod and Piran [16] and Gundlach [17] to independently predict and numerically verify the existence of fine structure in mass scaling beyond the critical exponent. The mass of resultant black holes is more fully described by the relation

$$ln(M_{BH}) = \gamma ln|p - p^*| + \Xi[ln|p - p^*|] + c_f \tag{4}$$

where Ξ is a periodic function with a universal period $\varpi = \Delta/(2\gamma) \approx 4.6$.

Shortly after Choptuik's paper, in an effort to study critical phenomena in more generic systems, Abraham and Evans [18] demonstrated similar behavior in the vacuum collapse of axisymmetric linearized gravitational waves. Since then, the goal of understanding fully nonlinear axisymmetric vacuum collapse (Brill [19] wave collapse) has been pursued, in broad terms, using both Finite Difference (FD) [20, 21, 22, 23] and spectral methods [23, 24, 25]. In the current paper, we take a first step in exploring the use of Discontinuous Galerkin (DG) methods [26] in this endeavor.

Discontinuous Galerkin acts as a hybrid between finite difference and spectral methods [27]. FD has as an advantage the locality in its definition of solutions and operators, allowing local refinement in areas with sharp features. Spectral methods, on the other hand, are global in the definition of operators and solutions which in general allows for higher accuracy with fewer degrees of freedom. DG represents a middle ground between the two by having discrete elements that allow for local definitions and refinements. However, it maintains flux terms between the elements and definitions of solutions and operators that hold across entire elements to regain some of the advantageous global properties characteristic of spectral methods.

To date, the DG method has not been widely used in published studies specifically targeting gravitational critical phenomena. Since Choptuik's work, most studies of critical phenomena have relied on FD methods using the adaptive mesh refinement (AMR) technique for resolving features near the critical point. In addition, computational studies have usually been performed in spherical symmetry, or at most axisymmetry, for reasons of computational tractability. However, DG has been used in related areas including general relativistic hydrodynamics [28, 29, 30], *e.g.* in the modeling of neutron star mergers. The high-order accuracy [31] of the DG method could be beneficial for resolving fine-scale structure in critical phenomena.

We anticipate several challenges in implementing the Discontinuous Galerkin method in critical phenomena studies, that we intend to address in this and future papers. DG is built for equations in conservative form, has difficulty with second-order operators, and there is currently a lack of robust tools suitable for DG in numerical relativity. In this paper, we choose Choptuik's original problem with a massless scalar field minimally coupled to gravity as a simple first case. This choice removes the problem of second-order operators, which we will address in future papers. In Section 2 we present a cursory solution to equations not in conservative form, however more complicated situations are not seen in this simple model. Overall, this paper serves

as an exploratory analysis of DG method's usefulness specifically in critical phenomena of gravitational collapse and as a stepping stone to a fully DG simulation of Brill wave collapse.

2. Methods

2.1. The Massless Scalar Field in Curved Spacetime

The minimally coupled massless scalar field satisfies the massless Klein-Gordon Equation:

$$\nabla_a \nabla^a \Phi = 0 \tag{5}$$

where ∇_a represents covariant differentiation.

Following Choptuik [12], we adopt a metric of the form:

$$ds^2 = -\alpha^2(r,t)dt^2 + a^2(r,t)dr^2 + r^2 d\Omega^2 \tag{6}$$

Defining the auxiliary variables:

$$\Psi = \frac{\partial \Phi}{\partial r} \tag{7}$$

$$\Pi = \frac{a}{\alpha}\frac{\partial \Phi}{\partial t} \tag{8}$$

we arrive at a set of evolution equations for the derivatives of Φ:

$$\frac{\partial \Pi}{\partial t} = \frac{1}{r^2}\frac{\partial}{\partial r}\left(\frac{r^2 \alpha}{a}\Psi\right) \tag{9}$$

$$\frac{\partial \Psi}{\partial t} = \frac{\partial}{\partial r}\left(\frac{\alpha}{a}\Pi\right) \tag{10}$$

Additionally, Einstein's Equations with stress-energy tensor

$$T_{ab} = \nabla_a \Phi \nabla_b \Phi - \frac{1}{2} g_{ab} \nabla_c \Phi \nabla^c \Phi \tag{11}$$

result in a set of constraints on the dynamical variables a and α, namely

$$\frac{1}{a}\frac{\partial a}{\partial r} + \frac{a^2 - 1}{2r} - 2\pi r\left(\Pi^2 + \Psi^2\right) = 0 \tag{12}$$

$$\frac{1}{\alpha}\frac{\partial \alpha}{\partial r} - \frac{1}{a}\frac{\partial a}{\partial r} - \frac{a^2 - 1}{r} = 0 \tag{13}$$

$$\frac{\partial a}{\partial t} = 4\pi r \alpha \Psi \Pi \tag{14}$$

2.2. Numerical Solutions of the Scalar Field Equations

For the studies presented in this paper, two independent codes were developed using the Discontinuous Galerkin and Finite Difference methods respectively. These codes are described in the subsections below. As a cross-check, we also made use of independent code developed by this group for previous publications [32, 33].

2.2.1. Non-dynamic Equations

Analysis begins by selection of an initial field $\phi(r, t = 0)$ from Table 1. In each case, the amplitude A is the parameter which is varied to study critical behavior. Time symmetry is assumed, that is $\Pi(r, t = 0) = 0$.

Family	Initial form of Φ
1	$\Phi(r) = A \exp\{-(r/5.35)^2\}$
2	$\Phi(r) = A \exp\{-(r-3)^2\}$
3	$\Phi(r) = A \tanh(r-3)$

Table 1: The initial conditions used for three different families for the scalar field, Φ

With this selection, initial data for the dynamical variables a and α is determined using Equations 12 and 13. This calculation is performed essentially the same way for both the DG and FD codes, using the fourth-order Runge-Kutta [34, 35] (RK4) method.

As a final condition to fix the coordinates, a is set to unity at the origin. This has the effect of defining the time t as the proper time of a central observer. Equation 12 is solved outward. Then, spacetime is assumed to be asymptotically Schwarzschild at the far boundary of the numerical domain and α is set to $1/a$. Elsewhere, α is obtained by integrating Equation 13 inward towards the origin. (Note that Equation 14 is used only for convergence testing in this analysis.)

This calculation is repeated at the end of each Runge Kutta stage of each time step described in Sections 2.2.2 and 2.2.3.

2.2.2. Discontinuous Galerkin Solution

For building a DG version of massless scalar field collapse, the deal.II library [36] was chosen due to it being an open source library with an active community and robust collection of tutorials. Built in capabilities of deal.II used in this analysis were: adaptive mesh refinement, dimension-agnostic

mesh structure (one can take advantage of symmetries by using fewer dimensions), and matrix free calculations. The matrix free format calculates matrix elements on the fly instead of pulling from memory to increase computational speed.

The method of solving Equations 9 and 10 follows much of the traditional DG approach. First, the equations need to be written in conservative form. Explicitly, the right hand side of Equation 9 is expanded out to a conservative form. Then, both sides are multiplied by a test function, v:

$$\int_{r_i}^{r_{i+1}} v\frac{\partial \Pi}{\partial t}dr = \int_{r_i}^{r_{i+1}} v\frac{\partial}{\partial r}\left(\frac{\alpha}{a}\Psi\right) + 2v\frac{\alpha\Psi}{ra}dr \tag{15}$$

$$\int_{r_i}^{r_{i+1}} v\frac{\partial \Psi}{\partial t}dr = \int_{r_i}^{r_{i+1}} v\frac{\partial}{\partial r}\left(\frac{\alpha}{a}\Pi\right)dr \tag{16}$$

Now the equations are integrated by parts to produce

$$\int_{r_i}^{r_{i+1}} v\frac{\partial \Pi}{\partial t}dr = \int_{r_i}^{r_{i+1}} -\frac{\partial v}{\partial r}\frac{\alpha}{a}\Psi + 2v\frac{\alpha\Psi}{ra}dr + v\frac{\alpha}{a}\Psi^*|_{r_i}^{r_{i+1}} \tag{17}$$

$$\int_{r_i}^{r_{i+1}} v\frac{\partial \Psi}{\partial t}dr = \int_{r_i}^{r_{i+1}} -\frac{\partial v}{\partial r}\frac{\alpha}{a}\Pi dr + v\frac{\alpha}{a}\Pi^*|_{r_i}^{r_{i+1}} \tag{18}$$

where Ψ^* and Π^* are the numerical flux. Since these equations form a linear system of hyperbolic equations, the Riemann conditions [27] must be solved to form the upwinding flux. This results in the following numerical fluxes where an upper index + indicates the value outside of the cell and an upper index of − indicates the value within the cell

$$c^* = \frac{\alpha^+\alpha^-}{a^+\alpha^- + a^-\alpha^+} \tag{19}$$

$$\Psi^* = c^*\left(\frac{a^+\Psi^+}{\alpha^+} + \frac{a^-\Psi^-}{\alpha^-} + \left(\Pi^+ - \Pi^-\right)\hat{n}^+\right) \tag{20}$$

$$\Pi^* = c^*\left(\frac{a^+\Pi^+}{\alpha^+} + \frac{a^-\Pi^-}{\alpha^-} + \left(\Psi^+ - \Psi^-\right)\hat{n}^+\right) \tag{21}$$

Ψ and Π are discretized as the sum of local discrete solutions of each

element, k.

$$\Psi(x,t) \simeq \bigoplus_{k=1}^{K} \Psi^k(x,t) \tag{22}$$

$$\Psi^k(x,t) \approx \sum_{n=1}^{N_E} \hat{\Psi}_n^k(t)\ell_n(x) \tag{23}$$

$$\Pi(x,t) \simeq \bigoplus_{k=1}^{K} \Pi^k(x,t) \tag{24}$$

$$\Pi^k(x,t) \approx \sum_{n=1}^{N_E} \hat{\Pi}_n^k(t)\ell_n(x) \tag{25}$$

Here, ℓ is a Lagrange polynomial and N_E is the total number of nodes within an element k.

Incorporating the discretizations along with defining the test function, v, as another Lagrange polynomial gives

$$\int_{r_i}^{r_{i+1}} \ell_i \ell_j dr \frac{\partial \Pi_j^k}{\partial t} = \int_{r_i}^{r_{i+1}} -\frac{\partial \ell_i}{\partial r}\frac{\alpha}{a}\Psi^k + 2\ell_i \frac{\alpha \Psi^k}{ra} dr + \ell_i \frac{\alpha}{a}\Psi^*|_{r_i}^{r_{i+1}} \tag{26}$$

$$\int_{r_i}^{r_{i+1}} \ell_i \ell_j dr \frac{\partial \Psi_j^k}{\partial t} = \int_{r_i}^{r_{i+1}} -\frac{\partial \ell_i}{\partial r}\frac{\alpha}{a}\Pi^k dr + \ell_i \frac{\alpha}{a}\Pi^*|_{r_i}^{r_{i+1}} \tag{27}$$

Both can be written as the linear system

$$M_{ij}\frac{\partial u_j^k}{\partial t} = b_i \tag{28}$$

The mass matrix ,M_{ij}, is block diagonal in DG allowing for more efficient matrix inversion. However, to maximize the benefits of DG, a change of basis was used to make the mass matrix diagonal and therefore trivially inverted [37].

Now both equations can be formed into an equation appropriate for explicit Runge Kutta evolution. DG is constrained by the need for a strong stability preserving Runge Kutta method. For these simulations, a fourth order, five stage Runge Kutta method was used [38]. One additional stage is needed when compared to the traditional Runge Kutta fourth order scheme; however, the formulation is built such that all stages don't need to be saved independently, low storage Runge Kutta, to further optimize the evaluation.

With the evolution of the dynamic variables set, the evolution of the adaptive mesh remains. At the end of every time step, a simplistic measurement of error was calculated for every cell in the mesh. If the error was greater than a user prescribed tolerance, the time step was thrown out and all cells that had error greater than the prescribed value are flagged for refinement. In addition, any cell with error less than the user specified value by a factor of 40 are flagged for coarsening. Then, the mesh was refined and coarsened following cell flags. The scalar field variables, Ψ and Π, were then interpolated from the old mesh to the new more refined mesh. Next, the non-dynamic equations were solved as prescribed in Section 2.2.1. Finally, the original time step is repeated with the more refined data. For the simplistic measure of error in a cell, the L^2-norm of the left hand side of Equation 13 was used.

Importantly, the integral for the L^2-norm of the left hand side of Equation 13 did take into account the physical structure of the simulation, meaning the spherical integrand term, r^2dr, was included here. This is different from all other integrals in this method and different from the simplistic measurement of error used in FD. The difference was needed as DG was unable to resolve the critical point without the change. This is believed to be because of the difference between dampening between the two methods. FD employs an ad hoc solution of Kreiss-Oliger dampening. This DG code employed no ad hoc dampener. The dampening came from the numerical flux, which was derived from the partial differential equations themselves. This may have allowed small errors from the outer region of the mesh to propagate inwards, growing as they did due to the spherical symmetry. Changing the simplistic measure of error to properly weigh regions in accordance with the underlying geometry resolved all issues.

2.2.3. Finite Differencing Solution

For the fully adaptive FD code, the domain is subdivided into a binary tree of cells, each containing of uniform grid of nodal points storing the value of each field. The spatial derivatives in Equation 9 and Equation 10 are computed via uniform 4th order centered finite difference stencils, interpolating values from neighboring cells as needed. This system is then integrated in time using the traditional RK4 method, with 5th-order Kreiss-Olgier dissipation to dampen out spurious numerical oscillations and ensure long-term stability.

Π is an even function and Ψ is an odd function, which is strongly enforced

on the inner boundary via ghost nodes. For the outer boundary, the code uses asymmetric stencils in order to approximate spatial derivatives. The code also applies Sommerfeld boundary conditions to allow outgoing wavefronts to pass through the boundary with minimal reflection [39].

$$\partial_t f = -\left[\partial_r f + \frac{f - f_0}{r}\right]. \tag{29}$$

Here Φ_0 and Π_0 are both taken to be 0.

In order to perform adaptive mesh refinement, an interpolating wavelet-based refinement criterion inspired by Fernando et al. [40] is used. For a cell on a given level, each node either coincides with a node on the next coarsest level or is the midpoint of two nodes on the next coarsest level. The detail coefficients of a cell are defined to be the difference between the value of a function at each a midpoint and the value found by interpolating that function from points on the next coarsest level. Every 20 times steps the code computes these detail coefficients on each cell. If the maximum detail coefficient on a cell is below a coarsening threshold (10^{-10}) or above a refinement threshold (10^{-8}), the code flags that cell for coarsening or refinement respectively. This refinement criterion focuses computational resources in regions with large spatial variation, and bounds error introduced by the FD stencil approximations.

3. Results

3.1. Mass Scaling

For all three families, the amplitude was varied in order to find a singular point, the critical point, separating black hole formation and dispersion of the scalar field. Figures 1 and 2 show the mass scaling relations for all three different families using both FD and DG methods. All figures are on a logarithmic scale so that the critical exponent, γ, can be extracted as the slope. A best fit was performed to a simple straight line. The approximate error of slopes in Figure 1 is .0003. The approximate error of slopes in Figure 2 is .002. The errors were determined by fitting a straight line to the data, separating the data into regions of similar variance from the fit, setting the error in those regions to be root mean square of the residuals, repeating the process three times, and using the variance of the final fit to determine approximate error. More accurate fits are applied in Section 3.3 that account

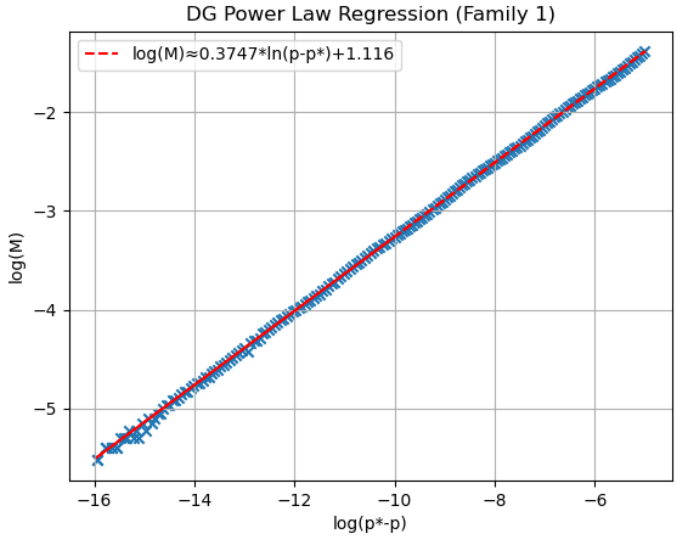

(a) Power law scaling of the black hole mass forming from a massless scalar field of Family 1 collapsing with 24 allowed refinement levels using DG.

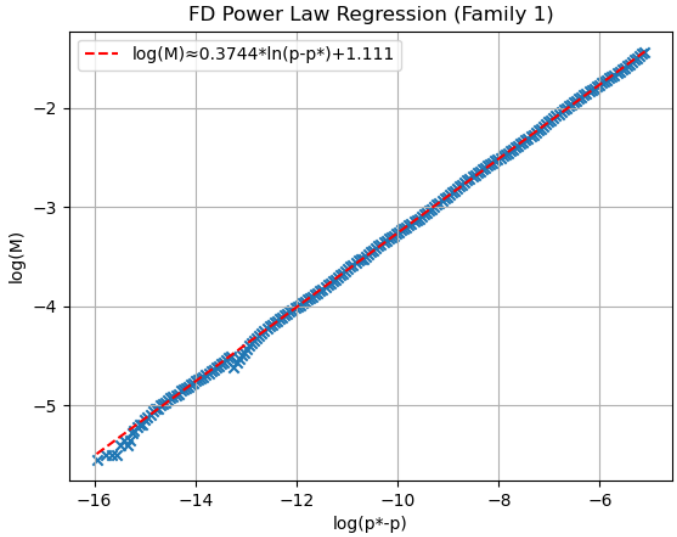

(b) Power law scaling of the black hole mass forming from a massless scalar field of Family 1 collapsing using a full adaptive refinement FD.

Figure 1: Comparison of power law scaling for Family 1 from Table 1. Up to 24 levels of refinement were allowed for these simulations. Which was the most performed for any run in this paper. Both slopes carry an error of approximately $\pm.0003$.

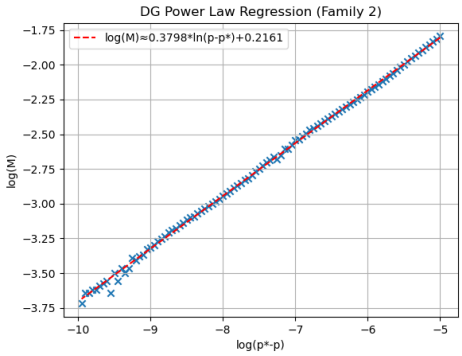

(a) Power law scaling of the black hole mass forming from a massless scalar field of Family 2 collapsing with 19 allowed refinement levels using DG.

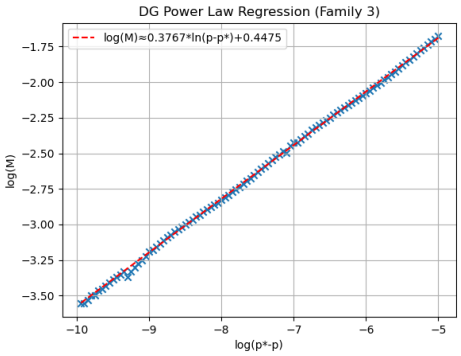

(b) Power law scaling of the black hole mass forming from a massless scalar field of Family 3 collapsing with 19 allowed refinement levels using DG.

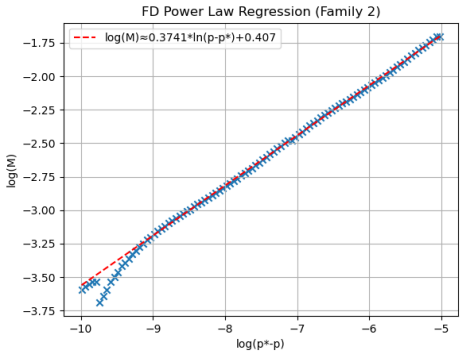

(c) Power law scaling of the black hole mass forming from a massless scalar field of Family 2 collapsing using a full adaptive refinement FD.

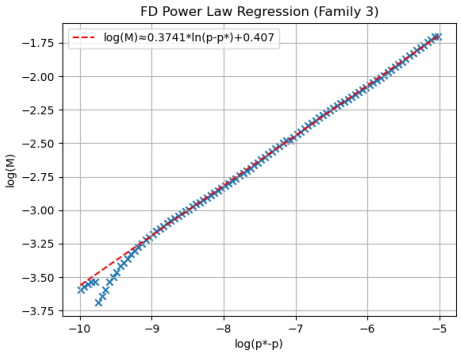

(d) Power law scaling of the black hole mass forming from a massless scalar field of Family 3 collapsing using a full adaptive refinement FD.

Figure 2: Collection of power law scaling for families 2 and 3 from Table 1. Columns correspond with the families and rows correspond with the codes used to run the simulations. The first row used the DG code, the second used the new adaptive FD code. These were run with lower allowed max refinement of 19. All slopes carry an approximate error of $\pm.002$.

for fine structure. Regardless of process, for both methods and all families, the slopes agree well with the accepted value of $\gamma \approx 0.37$ [41] and appear to be universal. Most notable is the difference in behavior between the two methods as the adaptive meshes approach their limits. This is seen in the points closest to criticality. FD results have a 'droop' that occurs twice in the FD graph of Figure 1 and once at the far left of both FD graphs in Figure 2. DG results in these same regions also experiences some instability. However, the instability appears more like randomized noise instead of falling off the trend line before abruptly rejoining. This appears to be caused by the difference in dampening or different refinement weights as explained in Section 2.2.2.

3.2. Discrete Self Similarity

Figure 3 shows the value of the scalar field, Φ, plotted with respect to the negative of logarithmic time, τ. (The negative is so that, more naturally, time increases going right.) The amplitude was chosen to be the largest amplitude of a dispersing field for the respective methods. As can be seen, this produces a figure with periodic behavior. The wavelength of this behavior is the discrete spacing of self similarity, Δ, also called the echoing constant [41].

To determine the error associated with the echoing constant, the wavelength was measured at three different points, as shown in Figure 3. The reported values are the average and standard deviation of those measurements. The wavelength measurement was performed at extrema, avoiding the beginning and end of the evolution as strong field dynamics did not dominate at these moments. For DG, $\Delta = 3.458 \pm 0.017$. This is in line with the expected value of $\Delta \simeq 3.44$ [41]. FD methods also agree with a measured value of $\Delta = 3.459 \pm 0.018$. No significant difference has been noted between the two methods.

3.3. Fine Structure

Data was fit to a model of $y = mx + b + A\cos(\omega x + p)$ for both methods. Data farther away from the critical point was used to minimize numerical noise. The linear terms were removed both from the data and best fit line to produce Figure 4.

From the best fit of the DG data, values for the critical exponent and fine structure wavelength were extracted, $\gamma = 0.37408 \pm 0.00002$ and $\varpi = 4.6283 \pm .0039$. An additional value for ϖ can be calculated using the stated relation $\varpi = \Delta/(2\gamma)$ using $\Delta = 3.458 \pm .017$ from Section 3.2

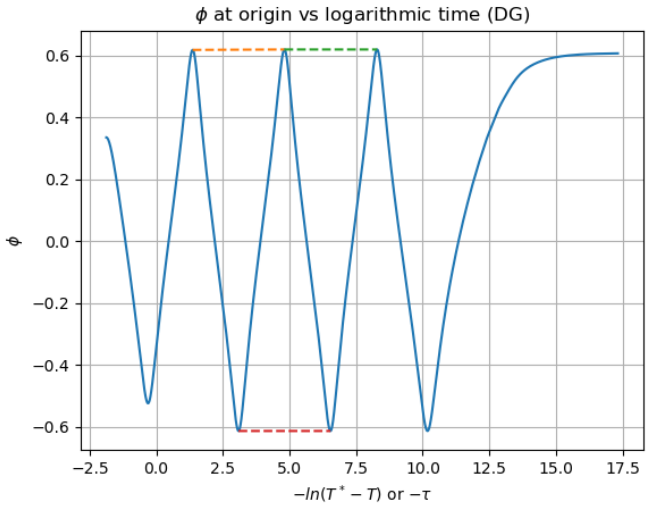

(a) The value of the scalar field, Φ, at the origin as seen by a central observer for the largest amplitude sub-critical DG run.

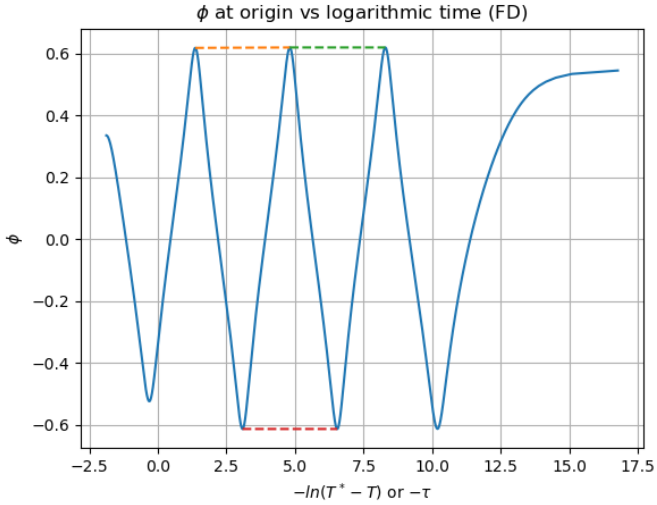

(b) The value of the scalar field, Φ, at the origin as seen by a central observer for the largest amplitude sub-critical FD run.

Figure 3: As strong field dynamics take hold, an echoing can be seen as the formation of periodic behavior that then tapers off as the sub-critical field disperses. Colored lines represent the three different spots the echoing constant was measured to account for the average and error bars.

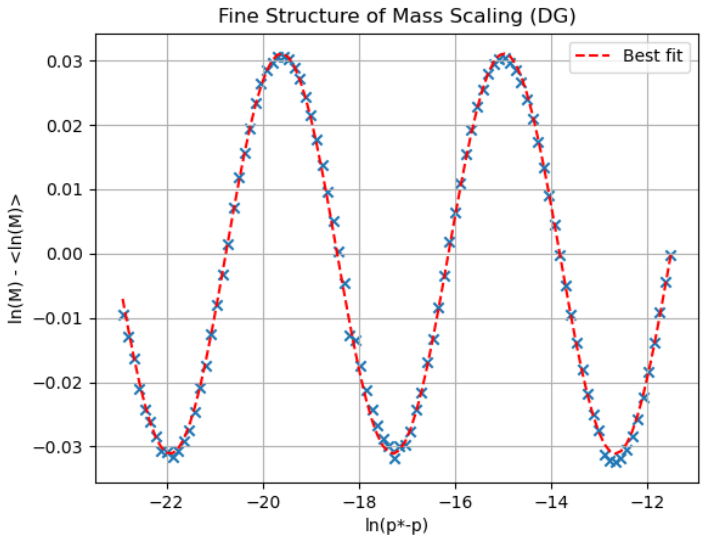

(a) Image of the fine structure of the mass scaling seen in the DG simulations.

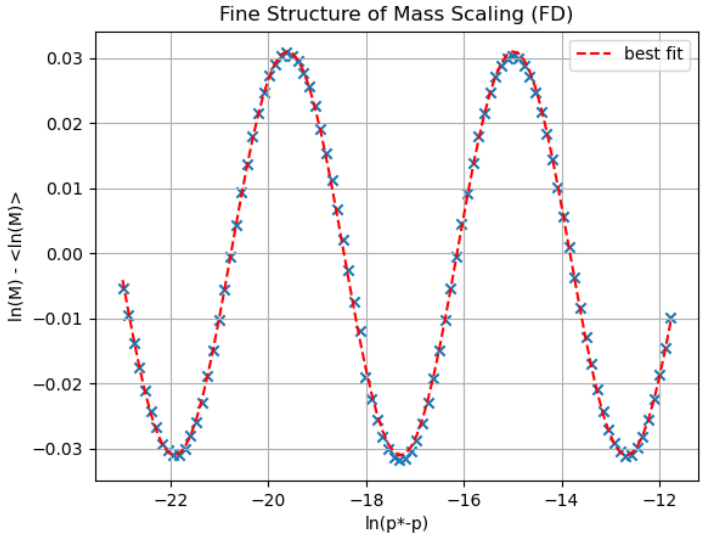

(b) Image of the fine structure of the mass scaling seen in the FD simulations.

Figure 4: The figure shows the periodic behavior of the fine structure of the mass scaling for both methods. For the y-axis, $< ln(M) >$ represents the linear terms of the best fit, following the same format as Hod and Piran [16]

.

as $\varpi = 4.622 \pm .022$. Both values for ϖ agree with each other and the expected value of $\varpi \approx 4.6$ [16, 17].

Repeating the same process for the FD data leads to measurements of $\gamma = .37408 \pm 0.00002$ and $\varpi = 4.62222 \pm 0.0029$. Again, this measured value of ϖ agrees with the calculated value using the relation between Δ and γ, $\varpi = 4.623 \pm 0.024$. Again, no serious difference is noticed between the two methods in the results.

3.4. Computation

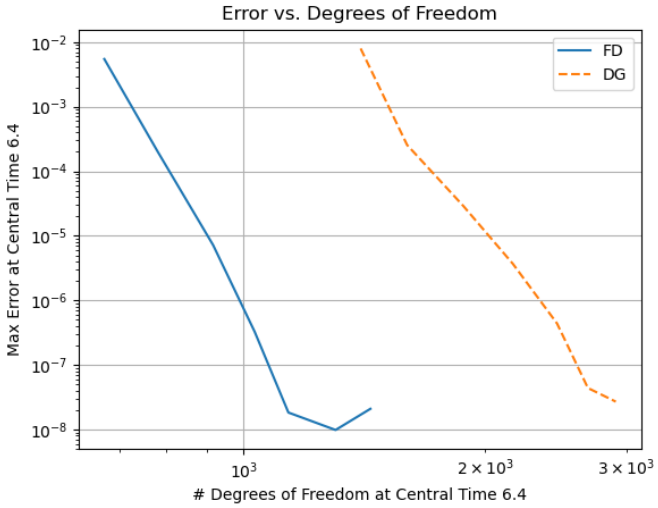

Figure 5: The L^∞-norm of the right hand side of Equation 14 of FD and DG methods run at maximum refinements allowed ranging from 9 to 16. The simulations were run until central observer time of 6.4, less than $T^* \approx 6.547$ for the family.

A comparison of convergence rates is shown in Figure 5. The figure shows the maximum error on the mesh at the same central observer time for simulations limited by a maximum refinement ranging from 9 to 16. Then, this value was plotted against the number of degrees of freedom at that moment. Error was measured as the violation of Equation 14 at each individual point. The central observer time, the proper time of an observer at $r = 0$, at the end of each run was 6.4 where $T^* \approx 6.547$, the earliest time of black hole formation, for the family used. Since the methods were both built to be fourth-order accurate and employed adaptive refinement, their respective

slopes should be less than -4 on the logarithmically scaled graph. The simulations were performed using Family 1 from Table 1 and an amplitude of 0.33603529, the critical point out to 8 significant figures. The number of significant figures matches the threshold used for refining cells, 10^{-8}. This also explains the end behavior of both lines. The point-wise error begins to approach the threshold, numerical noise then enters and causes the maximum error to oscillate near the limit.

Both methods have a slope less than -4 and are approximately equal. The largest difference is the number of degrees of freedom needed between the two methods. The difference of number of degrees of freedom is not representative of the comparison of the two methods since the runs stop short of T^*. The difference represents the initial overhead of DG.This initial difference is overcome as more accuracy is required, as will be shown in the ensuing figures. The cause of the initial overhead of DG is two-fold. First, DG double counts the degrees of freedom between cells to allow discontinuity. Second, the refinement process differs between the two methods as explained in Section 2.2.2. In particular, the DG refinement method assigned higher weights to points farther away from the origin than the FD method. Extra refinement in outer regions is caused by this difference, leading to more degrees of freedom being used.

The potential of DG is first seen in Figure 6. This graph represents a single run in both methods using Family 1 with the largest amplitude dispersing wave, where the number of degrees of freedom is plotted against the central observer time. Degrees of freedom are used as a heuristic for the necessary computational power, since this would correlate with the amount of storage and number of computations needed to be performed. DG initially uses more degrees of freedom, but is surpassed by FD as the simulation approaches the critical moment deciding between dispersion and collapse. The maximum number of degrees of freedom used by FD is 32% higher than that used by DG.

Figure 7 provides a better comparison between methods with relation to computational time. The figure again represents a single run in both methods using Family 1 with the largest amplitude dispersing wave. However, degrees of freedom are now plotted against the temporal step number. Temporal step number more accurately aligns with the proportion of the simulation expended at the corresponding degree of freedom. Both simulations were run to a central observer time of 6.55, just past the largest collapse time for Family 1, $T^* \approx 6.547$. This is done to capture the most computationally

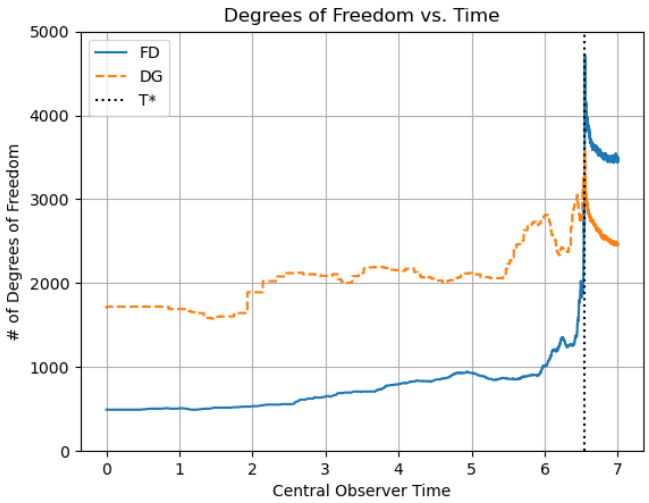

Figure 6: The total number of degrees of freedom used in the FD code and the DG code versus the time as seen by a central observer of the simulation using Family 1 and an amplitude of the largest dispersing wave of each method. The shortest collapse time,T^*, is indicated with a vertical line. This shows the initial overhead of DG and the ability of DG to overcome this overhead as more accuracy is needed.

demanding section of the simulation. Strikingly, the DG simulation 49% fewer steps than FD. Compounding upon the advantage of fewer steps, DG also used fewer degrees of freedom on average. The mean number of degrees of freedom per step for DG was 3134.4, whereas FD used 3256.6 degrees of freedom on average. This suggests that not only does DG take significantly fewer steps, but they are slightly less computationally intensive steps as well.

Figure 8 aids in demonstrating where the large difference in step numbers comes from. This figure again uses the same runs from the previous two figures. Now, the refinement level is contrasted with the step number. Increasing the level of refinement will decrease the smallest size of a cell by a factor of two. Since the Courant-Friedrichs-Lewy condition [42] demands the temporal step be smaller than the length of the smallest cell, a larger refinement level produces a slower moving simulation. Figure 8 clearly shows that the DG simulation, proportionally, spends more of the simulation at lower refinement levels. The difference in necessary refinement levels signals the ability of DG to resolve complex solutions with fewer degrees of freedom. The benefits would grow with higher demands of accuracy and increase in

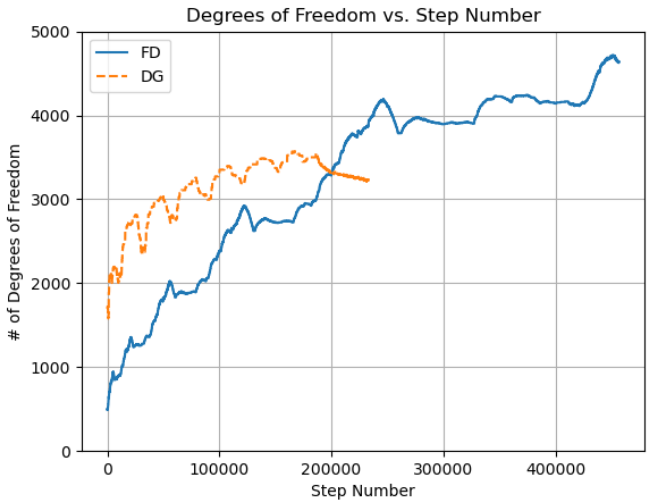

Figure 7: The total number of degrees of freedom used in the FD code and the DG code versus the time step number of the simulation, using Family 1 and an amplitude of the largest dispersing wave. Both simulations were run to a central observer time of 6.55 with $T^* \approx 6.547$ for this family.

complexity of simulated fields.

It deserves repeating that these are heuristics for determining better methods computationally; however, the results suggest that the benefits of DG will grow for critical phenomena simulations in higher dimensions and of more complicated fields. Such simulations are frequently limited by precision and refinement levels which is where DG excels.

4. Conclusion

In the effort to extend the study of black hole critical phenomena to higher dimensions and more generic systems, the Discontinuous Galerkin method shows promise as an avenue for exploration. Although it does have a larger initial computational cost, the DG method closes that gap as more accuracy is needed, due to its hybrid nature. DG tends to refine less and need fewer degrees of freedom, both on average and at maximum, when compared to FD, leading to more efficient and accurate critical phenomena analyses. This system only contained first order operators and one dimension due to its symmetry. The benefits of DG address the limitations of FD in more

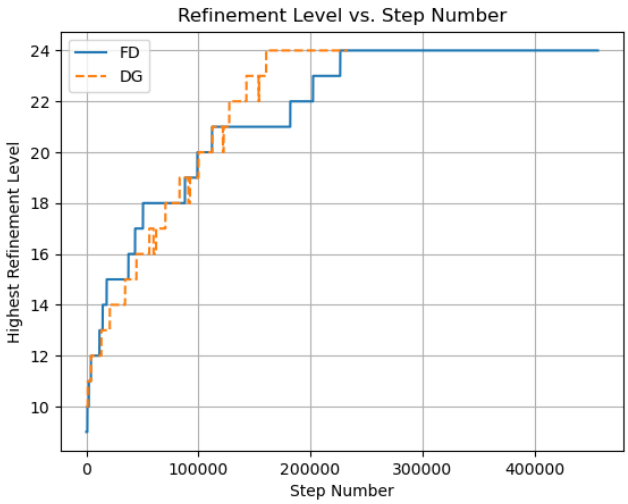

Figure 8: The highest level of refinement used in the FD code and the DG code versus the time step number of the simulation, using Family 1 and an amplitude of the largest dispersing wave. Both simulations were run to a central observer time of 6.55 with $T^* \approx 6.547$ for this family.

complicated systems, such as gravitational waves, and higher dimensions. However, handling higher order operators will be necessary as well in these more complicated systems. This will be discussed in a future paper.

5. Highlights

This will have to be moved to a separate file for submission.

Highlights should consist of 3 to 5 bullet points, each a maximum of 85 characters, including spaces.

Comparison of Discontinuous Galerkin and Finite Difference methods.

Discontinuous Galerkin methods use fewer degrees of freedom near criticality

Discontinuous Galerkin methods use half as many temporal steps near criticality

6. Acknowledgments

The work reported in this study has been supported by NSF grant PHY-2409629 and the University of Utah through the Office of the Dean of the

College of Science. We gratefully acknowledge the technical support and computational resources of the Center for High Performance Computing at the University of Utah. We thank Cole Kelson-Packer and Benjamin Derieg for valuable technical assistance.

References

[1] C. M. Will, The confrontation between general relativity and experiment, Living Reviews in Relativity 17 (4) (2014). doi:10.12942/lrr-2014-4.

[2] J. M. Weisberg, J. H. Taylor, The relativistic binary pulsar b1913+16: Thirty years of observations and analysis, in: F. A. Rasio, I. H. Stairs (Eds.), Binary Radio Pulsars, ASP Conference Series, Vol. 328, 2005, pp. 25–31.
URL `https://arxiv.org/abs/astro-ph/0407149`

[3] J. M. Weisberg, Y. Huang, Relativistic measurements from timing the binary pulsar psr b1913+16, The Astrophysical Journal 829 (1) (2016) 55. arXiv:1606.02744, doi:10.3847/0004-637X/829/1/55.

[4] B. P. Abbott, et al., Observation of gravitational waves from a binary black hole merger, Physical Review Letters 116 (6) (2016) 061102. doi:10.1103/PhysRevLett.116.061102.

[5] A. G. Riess, et al., Observational evidence from supernovae for an accelerating universe and a cosmological constant, The Astronomical Journal 116 (3) (1998) 1009–1038. doi:10.1086/300499.

[6] R. Penrose, Gravitational collapse and space-time singularities, Physical Review Letters 14 (3) (1965) 57–59. doi:10.1103/PhysRevLett.14.57.

[7] S. W. Hawking, R. Penrose, The singularities of gravitational collapse and cosmology, Proceedings of the Royal Society A 314 (1519) (1970) 529–548. doi:10.1098/rspa.1970.0021.

[8] P. S. Joshi, Gravitational Collapse and Spacetime Singularities, Cambridge University Press, 2007.

[9] S. B. Giddings, Black holes and massive remnants, Physical Review D 74 (10) (2006) 106005. doi:10.1103/PhysRevD.74.106005.

[10] R. Penrose, Gravitational collapse: The role of general relativity, Rivista del Nuovo Cimento 1 (1969) 252–276. doi:10.1007/BF02771419.

[11] S. L. Shapiro, S. A. Teukolsky, Formation of naked singularities: The violation of cosmic censorship, Physical Review Letters 66 (8) (1991) 994–997. doi:10.1103/PhysRevLett.66.994.

[12] M. W. Choptuik, Universality and scaling in gravitational collapse of a massless scalar field, Phys. Rev. Lett. 70 (1993) 9–12. doi:10.1103/PhysRevLett.70.9.
URL https://link.aps.org/doi/10.1103/PhysRevLett.70.9

[13] I. H. Dwivedi, P. S. Joshi, Naked singularities in spherically symmetric inhomogeneous tolman-bondi dust cloud collapse, Classical and Quantum Gravity 10 (12) (1993) 2359–2366. doi:10.1088/0264-9381/10/12/010.

[14] D. Christodoulou, Examples of naked singularity formation in the gravitational collapse of a scalar field, Annals of Mathematics 140 (3) (1994) 607–653. doi:10.2307/2118619.

[15] V. E. Hubeny, Overcharging a black hole and cosmic censorship, Physical Review D 59 (6) (1999) 064013. doi:10.1103/PhysRevD.59.064013.

[16] S. Hod, T. Piran, Fine structure of choptuik's mass-scaling relation, Physical Review D 55 (2) (1997) R440.

[17] C. Gundlach, Understanding critical collapse of a scalar field, Physical Review D 55 (2) (1997) 695.

[18] A. M. Abrahams, C. R. Evans, Critical behavior and scaling in vacuum axisymmetric gravitational collapse, Physical review letters 70 (20) (1993) 2980.

[19] D. R. Brill, On the positive definite mass of the bondi-weber-wheeler time-symmetric gravitational waves, Annals of Physics 7 (4) (1959) 466–483. doi:10.1016/0003-4916(59)90047-2.

[20] T. W. Baumgarte, C. Gundlach, D. Hilditch, Critical phenomena in the collapse of quadrupolar and hexadecapolar gravitational waves, Physical Review D 107 (8) (2023) 084012.

[21] M. W. Choptuik, E. W. Hirschmann, S. L. Liebling, F. Pretorius, An axisymmetric gravitational collapse code, Classical and Quantum Gravity 20 (9) (2003) 1857.

[22] E. Sorkin, On critical collapse of gravitational waves, Classical and Quantum Gravity 28 (2) (2011) 025011.

[23] T. W. Baumgarte, B. Brügmann, D. Cors, C. Gundlach, D. Hilditch, A. Khirnov, T. Ledvinka, S. Renkhoff, I. S. Fernández, Critical phenomena in the collapse of gravitational waves, Physical Review Letters 131 (18) (2023) 181401.

[24] D. Hilditch, A. Weyhausen, B. Brügmann, Evolutions of centered brill waves with a pseudospectral method, Physical Review D 96 (10) (2017) 104051.

[25] I. S. Fernández, S. Renkhoff, D. C. Agulló, B. Brügmann, D. Hilditch, Evolution of brill waves with an adaptive pseudospectral method, Physical Review D 106 (2) (2022) 024036.

[26] B. Cockburn, C.-W. Shu, The runge–kutta discontinuous galerkin method for conservation laws v: Multidimensional systems, Journal of Computational Physics 141 (2) (1998) 199–224. doi:https://doi.org/10.1006/jcph.1998.5892.
URL https://www.sciencedirect.com/science/article/pii/S0021999198958922

[27] J. S. Hesthaven, T. Warburton, Nodal Discontinuous Galerkin Methods: Algorithms, Analysis, and Applications, Springer, 2008. doi:10.1007/978-0-387-72067-8.

[28] L. E. Kidder, S. A. Teukolsky, B. Szilagyi, H. P. Pfeiffer, N. Deppe, M. A. Scheel, M. Zilhao, D. Radice, F. Foucart, R. Haas, Spectre: A task-based discontinuous galerkin code for relativistic astrophysics, Journal of Computational Physics 335 (2017) 84–114. arXiv:1609.00098, doi:10.1016/j.jcp.2017.01.027.

[29] D. Hilditch, M. Ruiz, M. Bugner, D. Löffler, B. Brügmann, The bamps code for numerical relativity, Classical and Quantum Gravity 33 (12) (2016) 125009. arXiv:1601.05597, doi:10.1088/0264-9381/33/12/125009.

[30] D. Radice, L. Rezzolla, Discontinuous galerkin methods for general-relativistic hydrodynamics: formulation and application to spherically symmetric spacetimes, Journal of Computational Physics 231 (3) (2012) 1061–1082. arXiv:1103.2420, doi:10.1016/j.jcp.2011.09.005.

[31] B. Cockburn, C.-W. Shu, Runge–kutta discontinuous galerkin methods for convection-dominated problems, Journal of Scientific Computing 16 (3) (2001) 173–261. doi:10.1023/A:1012873910884.

[32] C. Kelson-Packer, J. Belz, Investigation into length scale dominance in critical black hole formation, Physical Review D 102 (8) (2020) 084050.

[33] C. Kelson-Packer, J. Belz, Boundary dynamics in competing critical black hole formation, Physical Review D 106 (2022) 084063.

[34] W. H. Press, S. A. Teukolsky, W. T. Vetterling, B. P. Flannery, Numerical Recipes: The Art of Scientific Computing, 3rd Edition, Cambridge University Press, 2007.

[35] J. C. Butcher, Numerical Methods for Ordinary Differential Equations, 3rd Edition, John Wiley & Sons, 2016.

[36] P. C. Africa, D. Arndt, W. Bangerth, B. Blais, M. Fehling, R. Gassmöller, T. Heister, L. Heltai, S. Kinnewig, M. Kronbichler, M. Maier, P. Munch, M. Schreter-Fleischhacker, J. P. Thiele, B. Turcksin, D. Wells, V. Yushutin, The deal.ii library, version 9.6, Journal of Numerical Mathematics 32 (4) (2024) 369–380. doi:10.1515/jnma-2024-0137.

[37] M. Kronbichler, S. Schoeder, C. Müller, W. A. Wall, Comparison of implicit and explicit hybridizable discontinuous galerkin methods for the acoustic wave equation, International Journal for Numerical Methods in Engineering 106 (9) (2016) 712–739. arXiv:https://onlinelibrary.wiley.com/doi/pdf/10.1002/nme.5137, doi:https://doi.org/10.1002/nme.5137.
URL `https://onlinelibrary.wiley.com/doi/abs/10.1002/nme.5137`

[38] C. A. Kennedy, M. H. Carpenter, R. Lewis, Low-storage, explicit runge–kutta schemes for the compressible navier–stokes equations, Applied Numerical Mathematics 35 (3) (2000) 177–219.

doi:https://doi.org/10.1016/S0168-9274(99)00141-5.
URL https://www.sciencedirect.com/science/article/pii/S0168927499001415

[39] A. Sommerfeld, Die greensche funktion der schwingungslgleichung., Jahresbericht der Deutschen Mathematiker-Vereinigung 21 (1912) 309–352.

[40] M. Fernando, D. Neilsen, Y. Zlochower, E. W. Hirschmann, H. Sundar, Massively parallel simulations of binary black holes with adaptive wavelet multiresolution, Physical Review D 107 (6) (Mar 2023). doi:10.1103/physrevd.107.064035.

[41] C. Gundlach, J. M. Martin-Garcia, Critical phenomena in gravitational collapse, Living Reviews in Relativity 10 (2007) 1–57.

[42] R. Courant, K. Friedrichs, H. Lewy, Über die partiellen differenzengleichungen der mathematischen physik, Mathematische annalen 100 (1) (1928) 32–74.